Resolving the nanostructure of plasma-enhanced chemical vapor deposited nanocrystalline SiO_x layers for application in solar cells

M. Klingsporn, S. Kirner, C. Villringer, D. Abou-Ras, I. Costina, M. Lehmann, and B. Stannowski

Citation: Journal of Applied Physics **119**, 223104 (2016); doi: 10.1063/1.4953566
View online: http://dx.doi.org/10.1063/1.4953566
View Table of Contents: http://aip.scitation.org/toc/jap/119/22
Published by the American Institute of Physics

Resolving the nanostructure of plasma-enhanced chemical vapor deposited nanocrystalline SiO_x layers for application in solar cells

M. Klingsporn,[1] S. Kirner,[2] C. Villringer,[3] D. Abou-Ras,[4] I. Costina,[1] M. Lehmann,[5] and B. Stannowski[2]

[1]*IHP, Im Technologiepark 25, 15236 Frankfurt (Oder), Germany*
[2]*PVcomB, Helmholtz-Zentrum Berlin für Materialien und Energie, Schwarzschildstr. 3, 12489 Berlin, Germany*
[3]*Technische Hochschule Wildau, Hochschulring 1, 15745 Wildau, Germany*
[4]*Helmholtz-Zentrum Berlin für Materialien und Energie, Hahn-Meitner-Platz 1, 15109 Berlin, Germany*
[5]*Institut für Optik und Atomare Physik, Technische Universität Berlin, Straße des 17. Juni 135, 10623 Berlin, Germany*

(Received 14 January 2016; accepted 26 May 2016; published online 13 June 2016)

Nanocrystalline silicon suboxides (nc-SiO_x) have attracted attention during the past years for the use in thin-film silicon solar cells. We investigated the relationships between the nanostructure as well as the chemical, electrical, and optical properties of phosphorous, doped, nc-$SiO_{0.8}$:H fabricated by plasma-enhanced chemical vapor deposition. The nanostructure was varied through the sample series by changing the deposition pressure from 533 to 1067 Pa. The samples were then characterized by X-ray photoelectron spectroscopy, spectroscopic ellipsometry, Raman spectroscopy, aberration-corrected high-resolution transmission electron microscopy, selected-area electron diffraction, and a specialized plasmon imaging method. We found that the material changed with increasing pressure from predominantly amorphous silicon monoxide to silicon dioxide containing nanocrystalline silicon. The nanostructure changed from amorphous silicon filaments to nanocrystalline silicon filaments, which were found to cause anisotropic electron transport. *Published by AIP Publishing*. [http://dx.doi.org/10.1063/1.4953566]

I. INTRODUCTION

Amorphous silicon dioxide (a-SiO_2) and silicon suboxide (a-SiO_x) are well-established and understood materials with various applications such as insulators in semiconductor technology. During the past years, hydrogenated nanocrystalline silicon oxide (nc-SiO_x:H) fabricated by plasma enhanced chemical vapor deposition (PECVD) has been developed as a versatile material for use in silicon based solar cells, e.g., as an intermediate reflective layer (silicon oxide intermediate reflector, SOIR) in amorphous-silicon (a-Si:H)/microcrystalline-silicon (μc-Si:H) tandem solar cells that increases light harvesting in the a-Si:H top cell.[1–3] Since the electrical and optical parameters of the material are tunable within a wide range,[4] several other applications for solar cells have been explored. The material has been used as a transparent *n*-type[5] or *p*-type contact for heterojunction,[6,7] and thin-film silicon solar cells[8–11] or as a dielectric layer in back reflectors for a thin film single-junction[12] or double-junction solar cells.[13] For several years, spinodal decomposition of a-SiO_x layers by thermal annealing was used to fabricate silicon nanocrystals (nc-Si) in a silicon-dioxide matrix.[14–17] Moreover, the ability to control the size of the silicon nanocrystals in a silicon-dioxide matrix is indispensable in the study of quantum confinement effects.[14] Finally, nc-SiO_x is not only a versatile model system for studying quantum-dot networks but also a candidate material for silicon-based light-emitting diodes.[18]

Another approach for fabricating a-SiO_x:H and nc-SiO_x:H layers is a PECVD process with carbon dioxide as an oxygen source.[2,8,19] Using this source, Cuony *et al.*[8] found a significantly increased conductivity compared with other silicon oxides, which they related to the formation of a silicon rich phase. The authors later reported the growth of silicon nano-filament networks inside the nc-SiO_x:H material that led to strong electrical anisotropy.[20]

In addition to the [O]/[Si] ratio dependence of the filament formation, different approaches to tune the crystallinity were investigated, such as the influence of the hydrogen dilution[21] and the PECVD pressure.[22–24] Recent studies have also shown that the refractive index and conductivity can be tuned almost independently of each over a wide range.[25]

The nanocrystalline silicon growth during PECVD is usually explained by the competition and/or interaction of three distinct mechanisms. Atomic hydrogen, which is usually present in large quantities due to the high dissociation degree and large partial pressure (usually $>95\%$) of H_2, plays the key role in three all growth mechanisms. According to the chemical annealing model, atomic hydrogen diffuses into the growing surface and restructures bonds.[26] Furthermore, it covers the surface and thus enhances the adatom diffusion length[27] and preferably etches weak amorphous bonds at the same time.[28] The addition of the oxygen precursor has been observed to hinder the crystalline growth to some extent, making more extreme conditions in terms of hydrogen dilution and dissociation degree necessary. The total pressure is critical for optimizing the deposition process, because it influences the power density per molecule (thus dissociation), the particle residence time, which affects the gas depletion; and the potential difference

between the plasma bulk and sheath and therewith, the extent of ion bombardment. The reduction in a crystalline silicon volume fraction with higher deposition pressure observed in the samples studied here can be explained by either the higher silane depletion, which suppresses the atomic hydrogen annihilation reaction in the gas phase,[29] or reduced ion bombardment.[22]

While the refractive index is mainly determined by the [O]/[Si] ratio,[2] the conductivity depends on the nanostructure and the crystallinity. Therefore, a deeper understanding of the morphology and how the crystallinity influences the macroscopic electrical properties is of great interest for further device improvements and new potential applications. Until now, in most of the studies, the crystallinity of nc-SiO_x:H was treated as one of several dependent parameters and rarely as the sole subject of investigation.[22] In an earlier publication,[23] the macroscopic nc-SiO_x:H film properties, such as Raman crystallinity and refractive index, were correlated with the PECVD process and the plasma properties. In the present work, we unravel the nature of the nc-SiO_x:H nanostructure and correlate it to the macroscopic film properties and device behavior in the corresponding solar cells.

II. EXPERIMENTAL DETAILS

Phosphorous-doped, nc-SiO_x:H layers were deposited by PECVD using a fixed set of parameters and only by varying the deposition pressure between 533 and 1067 Pa. The layers were deposited in an Applied Materials AKT 1600 cluster tool[23] on $30 \times 30\,cm^2$ substrates at a temperature of 185 °C with 13.56 MHz plasma excitation frequency at a power of 500 W from process gases consisting of SiH_4 (10 sccm), H_2 (3000 sccm), CO_2 (18 sccm), and PH_3 (17.8 sccm). As illustrated in Fig. 1, three sets of samples were produced: nc-SiO_x:H layers with a thickness of 100 nm were deposited on two different substrates. Sample type A prepared on float glass substrates was used for conductivity measurements. Sample type B was grown on a float glass coated with 800 nm aluminum-doped zinc oxide (AZO) to

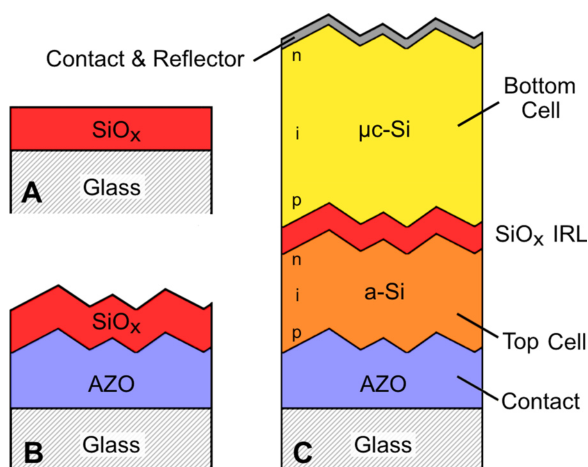

FIG. 1. Schematic diagrams of the three sample sets. (a) Sample type A: nc-SiO_x:H on glass for lateral conductivity measurements. (b) Sample type B: with an added AZO layer to avoid sample charging for XPS and ToF-SIMS and (c) a-Si:H/μc-Si:H tandem solar cell with a SOIR for device characterization.

avoid sample charging during X-ray photoelectron spectroscopy (XPS) and transmission electron microscopy (TEM) investigations. The last type of samples consisted of a 60 nm nc-SiO_x:H layer deposited as a SOIR between the top and bottom cell of a-Si:H/μc-Si:H tandem solar cells. Laser scribing was used to define separated 1 cm^2 solar cells.

The current-voltage *(I-V)* characteristics of the solar cells were measured using a dual-source (class AAA) WACOM sun simulator under standard test conditions. Illuminated IV curves were fitted using a one-diode model and the Lambert *W*-function approximation,[30] whereby the initial guesses for the series (R_s) and shunt (R_{sh}) resistances were calculated from derivatives at the axis crossings.[31]

Raman spectra were measured with a Renishaw InVia spectrometer with a 488 nm laser and a 50× objective. The laser power was carefully adjusted to avoid damaging the samples during the measurement process.

X-ray photoelectron spectroscopy experiments were carried out on a Physical Electronics PHI5000 Versa Probe II photoelectron spectrometer with a mono-chromated Al-K_α source operated in a high power mode at 100 W. To increase the probing depth, the takeoff angle was set to 85°. The Si2p peak was measured with a pass energy of 5.85 eV and 25 meV/step.

Spectroscopic ellipsometry (SE) was used to complement the analysis by XPS and Raman spectroscopy. SE can provide information about the crystalline volume fraction and the chemical composition, provided that the layer thickness and roughness are known well enough to develop an optical model. The ellipsometric parameters, namely, the amplitude component Ψ and phase difference Δ were recorded using a SENresearch SE 800 DUV 2C 16M ellipsometer at wavelengths ranging from 190 nm to 980 nm and at five angles between 50° and 70°. Transmission spectra measured over the same spectral region with a Perkin Elmer LAMBDA 1050 provided additional data.

The final fit was conducted for the range of 500–980 nm using an optical model of a surface/bulk/incubation layer stack.[32] Each layer was modeled as a mixture of silicon monoxide and silicon dioxide with Si inclusions using the Bruggemann effective medium approximation.[33] The two silicon monoxide and silicon dioxide matrix materials were individually modeled as Cauchy layers, while the nano-crystalline silicon inclusion material was modeled using three Gauss oscillators following the work of Gallas *et al.*[34]

For the TEM investigations, specimens were prepared from type B samples. Cross-sectioning was carried out conventionally by cutting, grinding, and subsequent ion milling. For the plan-view, preparation samples were scratched and immersed in 20% hydrochloric acid. After the AZO was etched away, the floating nc-SiO_x:H flakes with a thickness of 100 nm were collected with TEM copper grids. The analytical XTEM investigations were carried out on sample areas with a thickness of around 60 nm as determined by electron energy-loss spectroscopy (EELS). A FEI Tecnai Osiris instrument was used for analytical microscopy and the EELS data were acquired with the equipped Gatan Enfina FS-1 spectrometer in a scanning transmission electron

microscopy (STEM) mode. The energy resolution was determined as 1.1 eV by measuring the full width at half maximum (FWHM) of the zero-loss peak (ZLP). The data for the plasmon imaging were acquired by scanning the beam over the sample and acquiring one EEL spectrum per pixel with a sampling of 0.05 eV per channel. To reduce sample damage by the electron beam (e.g., knock-on damage, SiO_2 etching, and electron beam induced crystallization), a beam current of only 0.2 nA was used. The integration times were 10 ms–20 ms per spectrum, and the map size was 128 × 128 pixels[2] for an area of 128 × 128 nm^2. The resulting data cube was further evaluated using a self-developed software.

Energy dispersive x-ray spectroscopy (EDX) with a FEI ChemiSTEM^{TM} system, based on the Bruker Super-X EDX large angle detector array, was used to analyse the elemental distribution of the samples.

Selected area electron diffraction (SAED) was performed on plan-view samples by probing an area of 240 μm^2. The acquired ring patterns were further evaluated using the PASAD package[35] by subtracting a spline background and fitting the peaks with a pseudo-Voigt distribution. An estimation of the average coherent scattering domain size (D_{Avg}) was calculated by a Williamson-Hall plot[36] using the 111 and 220 reflections. High resolution TEM images were recorded with an image spherical aberration (C_s) corrected FEI Titan microscope operated at 300 kV.

III. RESULTS

A. Conductivity and solar-cell properties

IV curves of two solar cells are presented in Fig. 2. The device with a SOIR deposited at 533 Pa shows a pronounced s-shape in contrast to the curve of the device using the SOIR deposited at 800 Pa. The corresponding *IV* parameters of the solar cells as a function of the SOIR deposition pressure are shown in Fig. 3(a). The conversion efficiency displayed a strong pressure dependence. At 533 Pa, the SOIR was blocking under short circuit conditions corresponding to the lowest (lateral) conductivity in single nc-SiO_x:H layers, of below 10^{-11} S/cm (Fig. 3(b)). Higher deposition pressures resulted in a largely increased conductivity of the nc-SiO_x:H. The conversion efficiencies of the solar cells improved substantially to an average value of 11.7% at a deposition pressure of 800 Pa, where also R_s featured a minimum as depicted in Fig. 3(c). With increasing pressure, a small decrease in the average efficiency down to 11.2% at 1067 Pa was found.

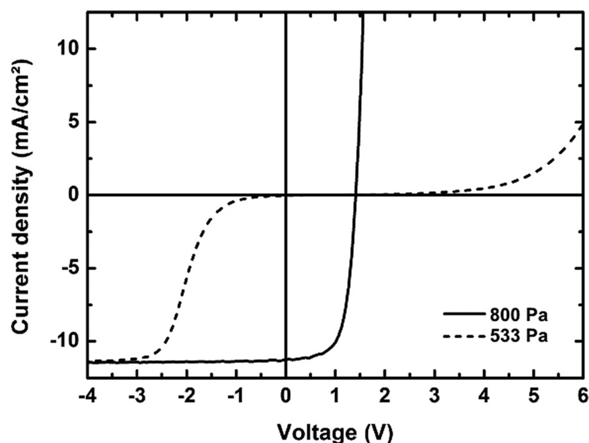

FIG. 2. Selected illuminated *IV* curves of tandem cells with nc-SiO_x:H SOIRs deposited at 533 Pa and 800 Pa. A strong S-shape, typical for defective tandem cells, was observed at 533 Pa. The *IV* curve of the 800 Pa cell is exemplary for the other cells (deposited at 567, 933, and 1067 Pa).

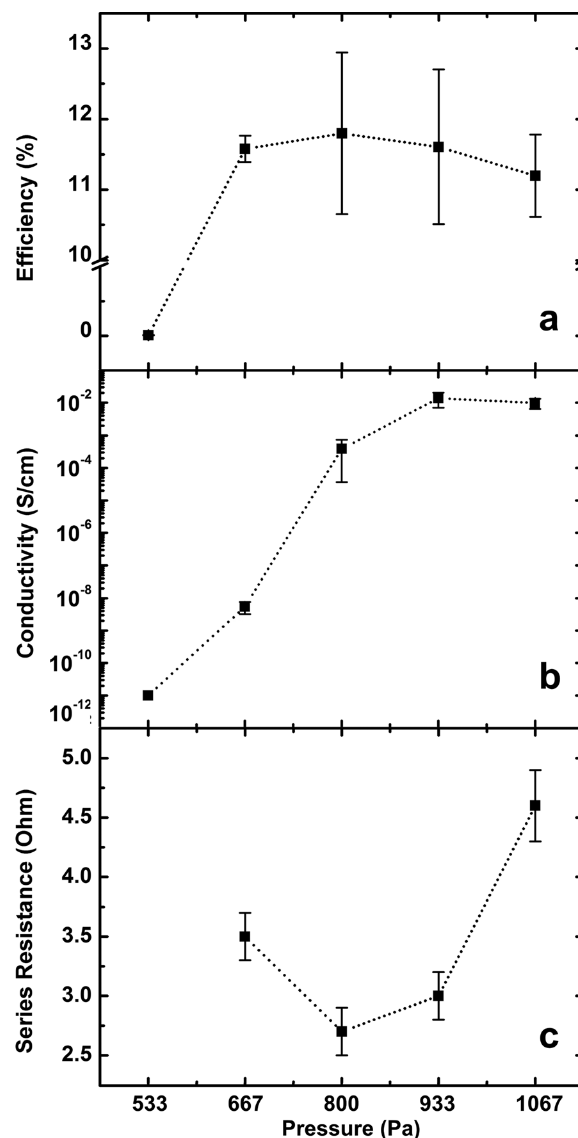

FIG. 3. Deposition pressure dependence of (a) power-conversion efficiency of the solar cells, (b) conductivity of sample type A, and (c) R_s determined from the fit of the *IV* curves.

B. Compositional results

The elemental composition of all samples over the pressure range of 533–1067 Pa was measured by plan-view EDX. The average [O]/[Si] ratio of the sample series was determined to be 0.8. Investigation of the chemical state of the silicon by XPS showed an oxidation induced splitting of the Si2p peak as depicted in Fig. 4. Analysis of the oxidation states was performed by deconvolution of the silicon 2p peak. It is known as a rule of thumb that the peak shifts 1 eV per oxidation state. The exact parameters were taken from Ref. 37 (Si^{1+}: 0.9 eV, Si^{2+}: 1.7 eV, Si^{3+}: 2.7 eV, Si^{4+}:

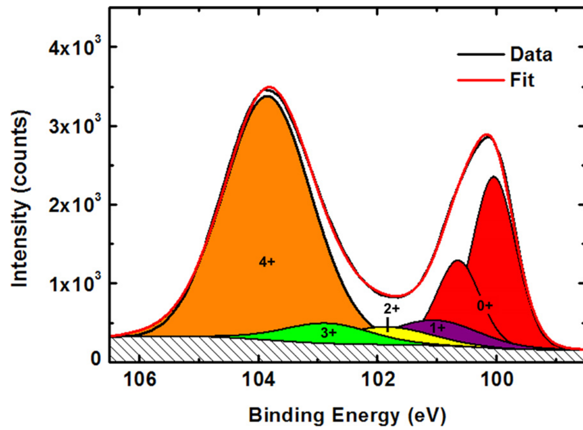

FIG. 4. Si2p peak photo-electron spectrum of a nc-SiO_x:H layer deposited at 933 Pa and the corresponding six-peak fit. It is seen that the sample mostly contains Si^{4+} (orange) and Si^0 (red), while a minor sub-oxide (green: Si^{3+}, yellow: Si^{2+}, purple: Si^{1+}) content is measured.

3.7 eV). To account for the spin-orbit coupling of the $Si2p^0_{1/2}$ and $Si2p^0_{3/2}$ states, two peaks about 0.6 eV apart were used for the elemental silicon. The deconvolution of the peak revealed the presence of silicon suboxides in the material. The observed evolution of the Si^{n+} distribution with increasing deposition pressure, despite the fixed oxygen content in the present study, indicates a phase separation. The silicon dioxide (Si^{4+}) fraction of the Si2p peak and the silicon oxide (Si^{1+} +, …, + Si^{4+}) fraction is shown in Fig. 5(a). While the overall amount of silicon oxides decreases from 0.76 to 0.72, the Si^{4+} fraction increases from 0.46 to 0.66.

Further analysis of the bulk composition by SE revealed a thin (∼5 nm) incubation layer at the AZO interface with a high fraction of silicon around 50%, a bulk layer of 75 nm–85 nm, and a 10 nm–15 nm top layer with increased oxide content. The resulting volume fractions of SiO, SiO_2, and Si are presented in Fig. 5(b) and indicate an increase in phase separation with pressure. Specifically, at 533 Pa, the SiO_x contains 76% SiO and only 7% Si, while with increasing pressure, the SiO fraction decreases to 9% while Si increases to 22% and SiO_2 to 69%. The refractive index of the bulk layer (at 632.8 nm) calculated with this model was found to be nearly constant (in average 2.06) with a deviation of 3%.

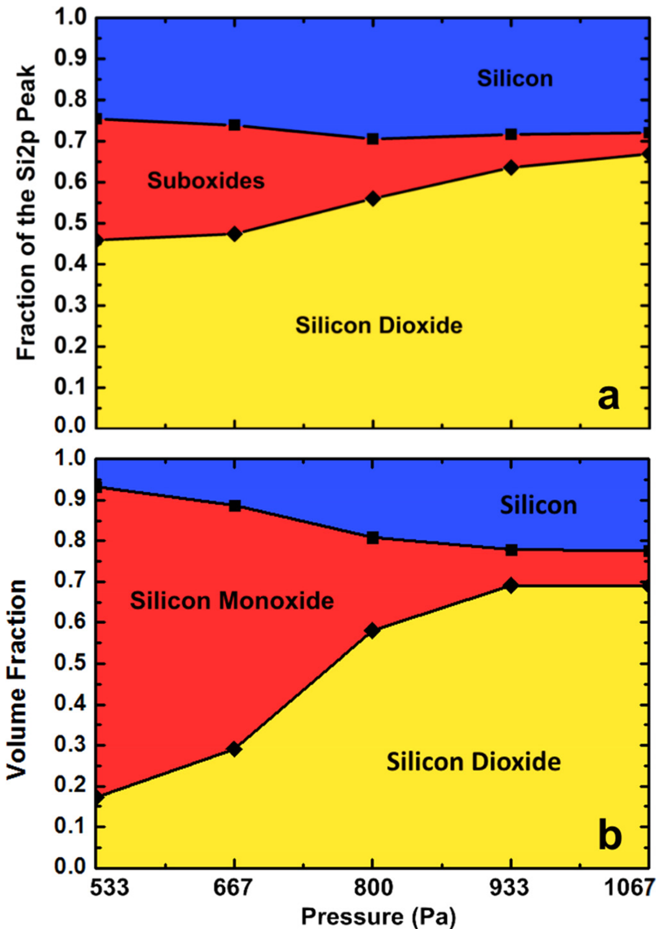

FIG. 5. (a) XPS: Evolution of the Si2p peak fraction with the deposition pressure regarding silicon Si^0 (blue), silicon suboxides Si^{1+}, Si^{2+}, Si^{3+} (red), and SiO_2 Si^{4+} (yellow). (b) SE: Evolution of the volume fraction of the nc-SiO_x:H showing the three components of the optical model: Si (blue), SiO (red), and SiO_2 (yellow).

C. Nanostructure

To resolve the nanostructure of nc-SiO_x:H, a specialized STEM-EELS analysis routine was employed. A single EEL spectrum of a nc-SiO_x:H layer deposited at 800 Pa is presented in Fig. 6. The evaluation routine for each EEL spectrum included the extraction of the single-scattering distribution (SSD) using the Fourier logarithm deconvolution[38] with the ZLP from the spectrum itself. The SSD was then fitted using a three-plasmon distribution of silicon, silicon monoxide, and silicon dioxide. The silicon dioxide and monoxide plasmon distribution was taken from reference samples. The Drude model was used to model the silicon plasmon with a plasmon energy of 17.1 eV, which corresponds to nc-Si with a diameter of 5 nm.[39] To rule out thickness effects, the ratio of the silicon plasmon loss to the low loss SSD spectrum in the range 10 eV–30 eV was mapped. By this technique, a lateral resolution of better than 1.5 nm has been already demonstrated.[40] The silicon plasmon ratio mappings obtained by this technique display the silicon nanostructure in the nc-SiO_x:H layers as shown in

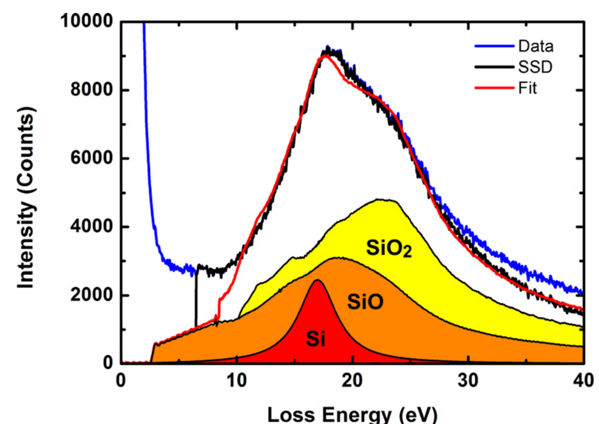

FIG. 6. Electron energy loss spectrum (blue) and the corresponding deconvoluted SSD (black) of a type B sample deposited at 800 Pa. The fit includes the Drude plasmon distribution for silicon (red) and the low loss references of SiO (orange) and SiO_2 (yellow).

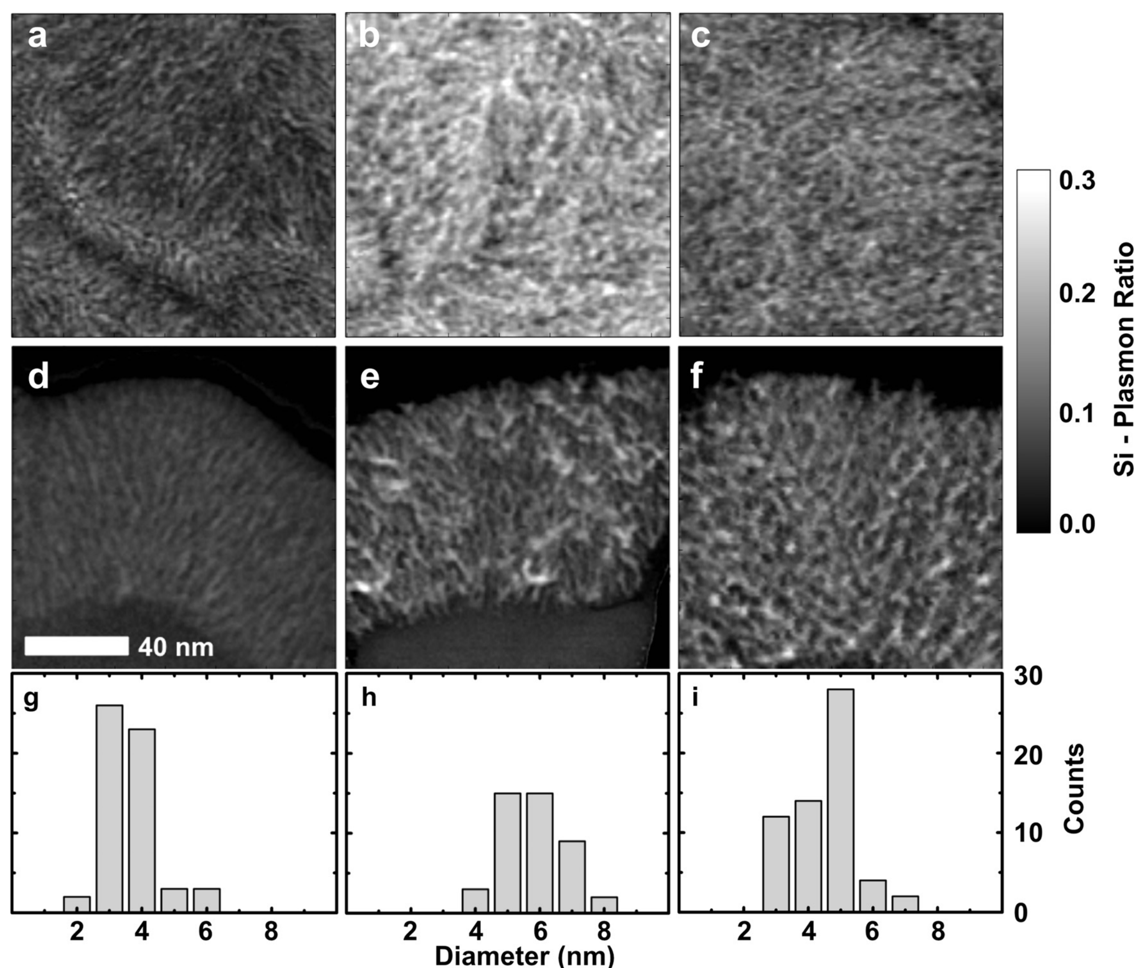

FIG. 7. STEM-EELS Si plasmon ratio mapping of plan-view (a)–(c) and cross-sectioned (d)–(f) nc-SiO_x:H layers deposited at (a), (d) 533 Pa, (e), (b) 800 Pa, (f), (c) 1067 Pa. (g)–(i) The corresponding distribution of the diameters was measured by linescans.

Figs. 7(a)–7(f). At 533 Pa (Figs. 7(a) and 7(d)), low intensity needle-like silicon filaments that are homogeneously distributed and oriented nearly perpendicular to the substrate are visible. At 800 Pa (Figs. 7(b) and 7(e)), thicker filaments with an average diameter of 5.2 nm with higher intensity become visible. From the plane-view, it is apparent that the silicon structures are not evenly distributed over the area and silicon poor areas are formed. At 1067 Pa (Figs. 7(c) and 7(f)), silicon filaments with a lower mean diameter of 3.9 nm form an evenly spread and isotropically interconnected network.

The HRTEM examinations of the nanostructure of nc-SiO_x:H layers validate the presence of silicon nanocrystals. An HRTEM image of a cross-sectioned nc-SiO_x:H type B layer deposited at 1067 Pa is presented in Fig. 8. The diameters of the silicon nanocrystals are in the order of 3 nm–5 nm. They are arranged in a pearl-chain like structure with short distances of often less than 1 nm between the crystallites.

D. Crystallinity

The SAED results for the series, presented in Fig. 10(a), confirmed the deposition pressure dependent formation of a nanocrystalline silicon phase in the material, at 667 Pa and higher pressures while no crystalline features are seen for 533 Pa. Results for the corresponding D_{Avg} calculated with Williams-Hall plots, depicted in Fig. 10(b), reveal an average size close to 6 nm for 667, 800, and 933 Pa and a drop to 3.8 nm at 1067 Pa.

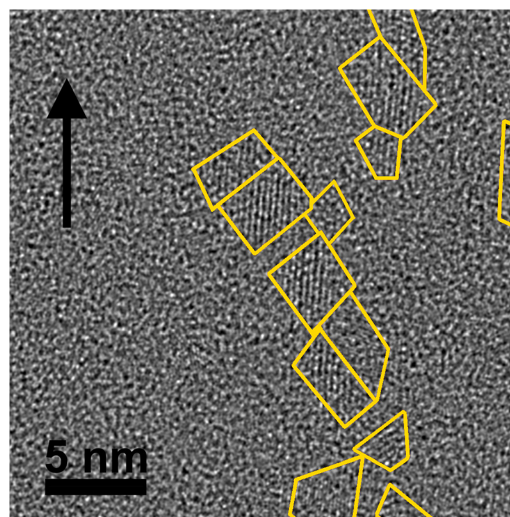

FIG. 8. C_s corrected HRTEM image of a cross-sectioned nc-SiO_x:H layer deposited at 1067 Pa. Silicon nanocrystals (marked yellow) form a pearl-chain like structure. The arrow indicates the growth direction of the layer.

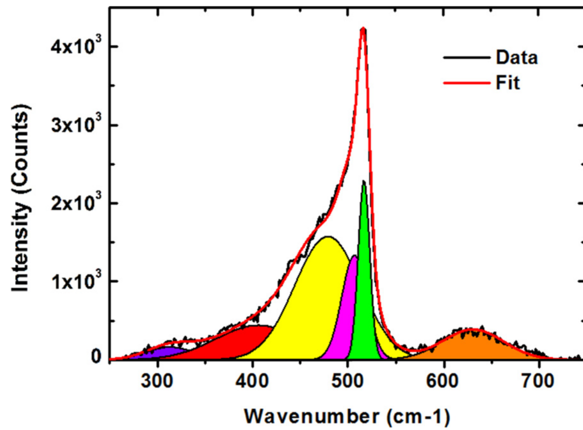

FIG. 9. Raman spectrum of a nc-SiO_x:H layer deposited at 933 Pa and the corresponding six peak fit. Two crystalline peaks at 510 cm^{-1} and 520 cm^{-1} are marked magenta and green and the amorphous peak at 480 cm^{-1} is marked yellow.

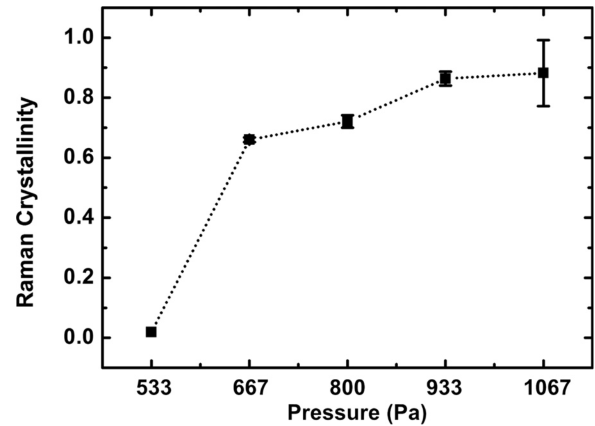

FIG. 11. Deposition pressure dependent Raman crystallinity with y calculated from D_{Avg}.

Raman crystallinity, as described by Bustarret *et al.*,[41] has been established as a quantitative standard measure for the fraction of crystalline silicon in silicon thin films. It is defined by the ratio of the Raman intensities associated with crystalline silicon (I_c) to the sum of intensities of crystalline silicon and intensities associated to amorphous silicon (I_a) weighted by the parameter y, to account for the differences in the scattering cross sections

$$F_c = I_c/(I_c + yI_a), \tag{1}$$

y is determined by the size of the silicon nanocrystals (L_{cry}) and the exponential decay factor (L_{eff})[41]

$$y(L_{cry}) = 0.1 + 0.9\exp(-L_{cry}/L_{eff}). \tag{2}$$

The Raman crystallinity was calculated in Eq. (1) after fitting the Raman spectra with six Gauss peaks as shown in Fig. 9. For L_{cry}, the values of D_{Avg} were used and L_{eff} was set 1 nm.[42] The results show the anticipated increase in F_c with increasing deposition pressure. As presented in Fig. 11, from a nearly amorphous F_c of 2% at a deposition pressure of 533 Pa, the value increases to a maximum of 88% at 1067 Pa.

IV. DISCUSSION

Detailed analysis of the chemical binding structure in PECVD deposited nc-SiO_x:H layers indicates that with increasing deposition pressures, the silicon structure changes from a predominantly continuous network of suboxides[43] with a Si^{n+} distribution roughly following the random bonding model,[44] towards a true two-phase system of silicon nanocrystals in a silicon dioxide matrix, as evidenced by Raman spectroscopy, SAED, and HRTEM. These findings were considered in an optical model used to fit the SE measurements. The same trend was found. Differences between the SE and XPS results at pressures below 800 Pa can be explained by a native oxide layer and the small probing depth of XPS of only a few nanometers.

Earlier investigations linked the high conductivity to the increased crystalline content[8] and the formation of silicon nano-filaments.[20] STEM-EELS plasmon imaging investigations confirmed the presence of silicon filaments as presented in Fig. 7. SAED investigations showed no signs of a crystalline phase at 533 Pa, which leads to the implication that the observed filaments consist of amorphous silicon. An nc-Si phase appears only in nc-SiO_x:H deposited at higher pressures. The amount of active dopants and the effective charge carrier mobility apparently improves drastically during the transition from the purely amorphous network to the partially crystalline one. Furthermore, the agglomeration of the nc-Si crystals into the pearl-chain like structure ("filament") allows a change in transversal conductivity of several orders of magnitude. Finally, no significant negative influence on the series resistance of the device from the SOIR can be observed and, as a result, the conversion efficiency of the solar cell increases to a high level.

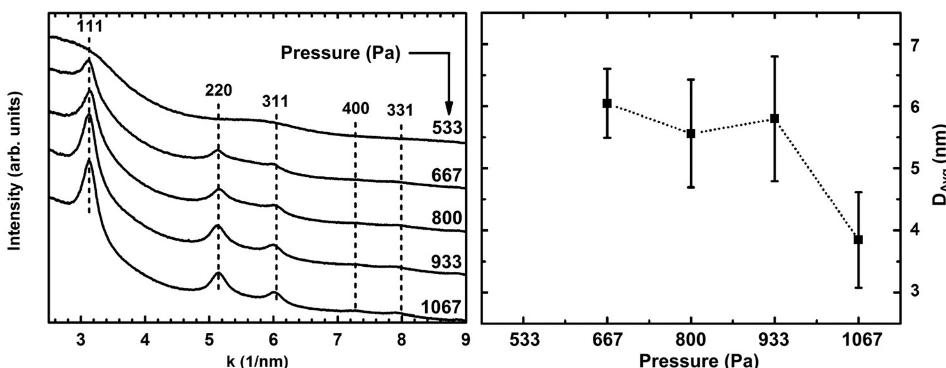

FIG. 10. (a) Intensity distribution of the SAED ring patterns of plan-view samples prepared from type B nc-SiO_x:H sample deposition pressure series. (b) Average coherent scattering domain sizes calculated from the corresponding Williamson-Hall plots.

Measurements of the average filament diameter in the Si plasmon ratio mappings at 800 Pa and 1067 Pa are in good agreement with the Williamson-Hall plot results. This indicates that the filaments consist of nc-Si. C_s corrected HRTEM measurements of nc-SiO_x:H validated this finding and showed that the microstructure of the filaments consists of a pearl-chain like structure of silicon nanocrystallites. With inter crystallite distances of often below 1 nm, the wave functions of the crystallites can overlap, forming energy bands[45] and allowing electron transport along the filaments.

With this, the drop in the power conversion efficiency from 800 to 1067 Pa despite the increase of the lateral conductivity can be understood. The change in structure from thicker filaments with silicon poor areas to a homogenous filament network without silicon poor areas causes the increase in lateral conductivity and the decrease in transversal conductivity, as can be deduced from comparison of R_S and the lateral conductivity. This shows the anisotropic, electrical properties of nc-SiO_x:H.

V. CONCLUSION

In the present study, we demonstrated that the crystallinity and nanostructure of PECVD deposited n-type nc-SiO_x:H can be tuned by the pressure during deposition without affecting the stoichiometry. While the refractive index is nearly independent of the pressure, the conductivity varies substantially for different deposition pressures. When increasing the deposition pressure from 533 to 1067 Pa, the (lateral) film conductivity changes over ten orders of magnitude from "insulating" to "conducting." This is caused by the film structure changing from a heterogeneous material with a small fraction of amorphous silicon filaments embedded in a silicon-suboxide matrix to a structure with a larger fraction of nanocrystalline silicon filaments embedded in a silicon dioxide matrix.

We showed that such crystalline filaments have a pearl-chain like structure of silicon nanocrystals. Nanocrystalline P-doped filaments were identified to be responsible for the crystallinity-dependent conductivity of nc-SiO_x:H. Furthermore, evidence for anisotropic transport was presented. nc-SiO_x:H films with low lateral conductivities ($<10^{-6}$ S/cm) resulted in solar-cell devices with a low series resistances, in contrast to nc-SiO_x:H films with a high transversal conductivities.

At low pressure, amorphous filaments are homogenously distributed in the film. With increasing pressure, the filament crystallinity and the diameter increase, but silicon-poor areas are also apparent. With further increasing pressure, the crystallinity of the filaments does not change significantly, but the filament density increases with a decreased average diameter—apparently forming an isotropically connected nc-Si filament network.

ACKNOWLEDGMENTS

This work was supported by the Federal Ministry of Education and Research (BMBF) and State Government of Berlin (SENBWF) in the framework of the program "Spitzenforschung und Innovation in den Neuen Ländern" (Grant No. 03IS2151). We also like to thank all people who made this work possible. Especially Onno Gabriel for the valuable discussions, Sonya Calnan for the AZO reference spectra, Jan Feldhoff and Wolfhard Fehre for all the Python tips and tricks, Ulrike Bloeck and Peter Schubert-Bischoff for their experience and help with the TEM sample preparation, Tore Niermann for HRTEM investigations, and Markus Wollgarten for the valuable discussions.

[1]A. Lambertz, A. Dasgupta, W. Reetz, A. Gordijn, R. Carius, and F. Finger, in Proceedings of the 22nd EUPVSEC (European Photovoltaic Solar Energy Conference), Milan, Italy, 3–7 September 2007.
[2]P. Buehlmann, J. Bailat, D. Dominé, A. Billet, F. Meillaud, A. Feltrin, and C. Ballif, Appl. Phys. Lett. **91**, 143505 (2007).
[3]S. Kirner, M. Hammerschmidt, C. Schwanke, D. Lockau, S. Calnan, T. Frijnts, S. Neubert, A. Schopke, F. Schmidt, J.-H. Zollondz, A. Heidelberg, B. Stannowski, R. Rech, and R. Schlatmann, IEEE J. of Photov. **4**, 10 (2013).
[4]V. Smirnov, A. Lambertz, B. Grootoonk, R. Carius, and F. Finger, J. Non-Cryst. Solids **358**, 1954 (2011).
[5]K. Ding, U. Aeberhard, V. Smirnov, B. Holländer, F. Finger, and U. Rau, Jpn. J. Appl. Phys., Part 1 **52**, 122304 (2013).
[6]J. Sritharathikhun, F. Jiang, S. Miyajima, A. Yamada, and M. Konagai, Jpn. J. Appl. Phys., Part 1 **48**, 101603 (2009).
[7]L. Mazzarella, S. Kirner, B. Stannowski, L. Korte, B. Rech, and R. Schlatmann, Appl. Phys. Lett. **106**, 023902 (2015).
[8]P. Cuony, M. Marending, D. T. L. Alexander, M. Boccard, G. Bugnon, M. Despeisse, and C. Ballif, Appl. Phys. Lett. **97**, 213502 (2010).
[9]K. Schwanitz, S. Klein, T. Stolley, M. Rohde, D. Severin, and R. Trassl, Sol. Energy Mater. Sol. Cells **105**, 187 (2012).
[10]M. Rohde, M. Zelt, O. Gabriel, S. Neubert, S. Kirner, D. Severin, T. Stolley, B. Rau, B. Stannowski, and R. Schlatmann, Thin Solid Films **558**, 337 (2014).
[11]V. Smirnov, A. Lambertz, and F. Finger, Energy Procedia **84**, 71 (2015).
[12]P. D. Veneri, L. V. Mercaldo, and I. Usatii, Appl. Phys. Lett. **97**, 023512 (2010).
[13]B. Janthong, A. Hongsingthong, T. Krajangsang, L. Zhang, P. Sichanugrist, and M. Konagai, J. Non-Cryst. Solids **358**, 2478 (2012).
[14]J. Heitmann, F. Müller, M. Zacharias, and U. Gösele, Adv. Mater. **17**, 795 (2005).
[15]E. C. Cho, S. Park, X. Hao, D. Song, G. Conibeer, S. C. Park, and M. Green, Nanotechnology **19**, 245201 (2008).
[16]J. J. van Hapert, A. M. Vredenberg, E. E. van Faassen, N. Tomozeiu, W. M. Arnoldbik, and F. H. P. M. Habraken, Phys. Rev. B **69**, 245202 (2004).
[17]X. Y. Chen, Y. Lu, L. J. Tang, Y. H. Wu, and B. J. Cho, J. Appl. Phys. **97**, 014913 (2005).
[18]M. F. Cerqueira, M. Stepikhova, A. Kozanecki, G. Andrês, and E. Alves, J. Nanosci. Nanotechnol. **10**, 2663–2668 (2010).
[19]S. Kirner, S. Calnan, O. Gabriel, S. Neubert, M. Zelt, B. Stannowski, B. Rech, and R. Schlatmann, Phys. Status Solidi C **9**, 2145 (2012).
[20]P. Cuony, D. Alexander, I. Perez-Wurfl, M. Despeisse, G. Bugnon, M. Boccard, T. Söderström, A. Hessler-Wyser, C. Hébert, and C. Ballif, Adv. Mater. **24**, 1182 (2012).
[21]A. Lambertz, T. Grundler, and F. Finger, J. Appl. Phys. **109**, 113109 (2011).
[22]S. Kirner, O. Gabriel, B. Stannowski, B. Rech, and R. Schlatmann, Appl. Phys. Lett. **102**, 051906 (2013).
[23]L. Mercaldoa, P. Veneria, I. Usatiia, E. Espositoa, and G. Nicotrab, Sol. Energy Mater. Sol. Cells **119**, 67 (2013).
[24]O. Gabriel, S. Kirner, M. Klingsporn, F. Friedrich, B. Stannowski, and R. Schlatmann, Plasma Processes Polym. **12**, 82 (2015).
[25]A. Lambertz, V. Smirnov, T. Merdzhanova, K. Ding, S. Haas, G. Jost, and U. Rau, Sol. Energy Mater. Sol. Cells **119**, 134 (2013).
[26]K. Nakamura, K. Yoshina, S. Takeoka, and I. Shimizu, Jpn. J. Appl. Phys., Part 1 **34**, 442 (1995).
[27]A. Matsuda, J. Non-Cryst. Solids **59**, 767 (1983).
[28]C. Tsai, G. Anderson, R. Thompson, and B. Wacker, J. Non-Cryst. Solids **114**, 151 (1989).
[29]M. Kondo, M. Fukawa, L. Guo, and A. Matsuda, J. Non-Cryst. Solids **266**, 84 (2000).
[30]A. Ortiz-Conde, F. García Sánchez, and J. Muci, Solid-State Electron. **44**, 1861 (2000).
[31]C. Zhang, J. Zhang, Y. Hao, Z. Lin, and C. Zhu, J. Appl. Phys. **110**, 064504 (2011).

[32]A. Samanta and D. Das, Appl. Surf. Sci. **259**, 477 (2012).
[33]D. A. G. Bruggeman, Ann. Phys. **416**(7), 636 (1935).
[34]B. Gallas, I. Stenger, C.-C. Kao, S. Fisson, G. Vuye, and J. Rivory, Phys. Rev. B **72**, 155319 (2005).
[35]C. Gammer, C. Mangler, C. Rentenberger, and H. Karnthaler, Scr. Mater. **63**, 312 (2010).
[36]G. Williamson and W. Hall, Acta Metall. **1**, 22–31 (1953).
[37]R. Alfonsetti, L. Lozzi, M. Passacantado, P. Picozzi, and S. Santucci, Appl. Surf. Sci. **70–71**, 222 (1993).
[38]F. Wang, R. Egerton, and M. Malac, Ultramicroscopy **109**, 1245 (2009).
[39]M. Mitome, Y. Yamazaki, H. Takagi, and T. Nakagiri, J. Appl. Phys. **72**, 812 (1992).
[40]G. Kissinger, D. Kot, M. Klingsporn, M. A. Schubert, A. Sattler, and T. Müller, ECS J. Solid State Sci. Technol. **4**(9), N124 (2015).
[41]E. Bustarret, M. A. Hachicha, and M. Brunel, Appl. Phys. Lett. **52**(20), 1675 (1988).
[42]S. Hernández, J. López-Vidrier, L. López-Conesa, D. Hiller, S. Gutsch, J. Ibáñez, S. Estradé, F. Peiró, M. Zacharias, and B. Garrido, J. Appl. Phys. **115**, 203504 (2014).
[43]A. Barranco, J. A. Mejías, J. P. Espinós, A. Caballero, A. R. González-Felipe, and F. Yubero, J. Vac. Sci. Technol., A **19**, 136 (2001).
[44]F. G. Bell and L. Ley, Phys. Rev. B **37**, 8383 (1988).
[45]S. Gutsch, J. Laube, A. M. Hartel, D. Hiller, N. Zakharov, P. Werner, and M. Zacharias, J. Appl. Phys. **113**, 133703 (2013).